

1 **Contrasting Aerosol Mixing States at Inland and Coastal Sites: An**
2 **Entropy-Based Metric for CCN Activity**

3 Jingye Ren^{1,2}, Wei Xu³, Ru-Jin Huang^{1*}, Fang Zhang^{4*}, Ying Wang¹, Lu Chen⁵, Jurgita
4 Ovadnevaite⁶, Darius Ceburnis⁶, Colin O'Dowd⁶, Yele Sun⁷

5 ¹*State Key Laboratory of Loess Science, Institute of Earth Environment, Chinese*
6 *Academy of Sciences, Xi'an, 710061, China,*

7 ²*Xi'an Institute for Innovative Earth Environment Research, Xi'an, 710061, China,*

8 ³*State Key Laboratory of Advanced Environmental Technology, Institute of Urban*
9 *Environment, Chinese Academy of Sciences, Xiamen, 361021, China,*

10 ⁴*School of Ecology and Environment, College of Artificial Intelligence, Harbin Institute*
11 *of Technology, Shenzhen, 518005, China,*

12 ⁵*School of Ocean and Geographic Science, Yancheng Teachers University, Yancheng*
13 *224051, China,*

14 ⁶*School of Natural Sciences, Centre for Climate & Air Pollution Studies, Ryan Institute,*
15 *University of Galway, University Road, Galway, Ireland,*

16 ⁷*State Key Laboratory of Atmospheric Boundary Layer Physics and Atmospheric*
17 *Chemistry, Institute of Atmospheric Physics, Chinese Academy of Sciences, Beijing*
18 *100029, China.*

19 Corresponding author: Ru-Jin Huang, rujin.huang@ieecas.cn; Fang Zhang,
20 zhangfang2021@hit.edu.cn

21

22

23

24

25 **Abstract**

26 Simplified assumptions of aerosol mixing states in modeling studies often
27 introduce substantial uncertainties in estimating cloud condensation nuclei (CCN)
28 concentrations (N_{CCN}) and their climatic impacts. This study systematically investigates
29 the contrasting relationships between mixing states and CCN activity by combining
30 field measurements of ~~probability distribution function of~~ the hygroscopicity
31 ~~distribution~~ with the algorithm of entropy at two inland and coastal sites. We show
32 distinct seasonal variations of aerosol mixing state. In winter, externally-mixed particles
33 dominated both sites, with comparable mixing state indices (χ) of 0.38 ± 0.12 and
34 0.39 ± 0.09 respectively for coastal air and inland air. However, ~~summer~~ measurements
35 ~~during summer periods~~ showed pronounced differences: ~~photochemical processes~~
36 ~~promoted significantly~~ aerosols in the coastal atmosphere exhibited a higher degree of
37 ~~internal mixing in coastal aerosols~~ ($\chi=0.69\pm 0.19$), whereas inland χ values only
38 increased moderately to 0.47 ± 0.12 . Aerosol mixing state is largely influenced by
39 primary emissions and secondary formation process. Externally-mixed particles
40 originate chiefly from anthropogenic emissions in inland or sea salt in coastal. During
41 the aging process, particles become more internally-mixed as the enhanced fraction of
42 more-hygroscopic mode. A universal logarithmic correlation was identified between
43 the critical diameter (D_{crit}) characterizing CCN activity and χ ($D_{crit} = -32.15\ln(\chi)+84.71$,
44 Pearson $r = -0.74$), but with distinct decrement rates for coastal vs. inland aerosols.
45 Further analysis reveals ~~a 0.1 increase in χ enhanced winter~~ the covariation relationships

设置了格式: 字体颜色: 自动设置

46 ~~between the mixing state and CCN activity; N_{CCN} by 39–65% at the supersaturation of~~
47 ~~0.2%, whereas this effect diminished exhibits heightened sensitivity to ~9% fluctuations~~
48 ~~in summers at low values.~~ These results underscore that mixing states exert different
49 control over N_{CCN} in diverse environments. Our work provides critical constraints for
50 parameterizing fine aerosols CCN activity in climate models.

设置了格式: 字体颜色: 自动设置

设置了格式: 字体颜色: 自动设置

设置了格式: 字体颜色: 自动设置

51
52
53

54 1. Introduction

55 Atmospheric cloud condensation nuclei (CCNs) are complex mixtures of organic
56 and inorganic components. Their chemical and physical properties make quantifying
57 aerosol-cloud interactions challenging (Liu et al., 2018; Rosenfeld et al., 2019; Xu et
58 al., 2022, 2024; Virtanen et al., 2025), introducing uncertainties into climate effect
59 assessments (Charlson et al., 1992; Shrivastava et al., 2017; IPCC, 2021; Chen et al.,
60 2022a; Manavi et al., 2025). Accurate climate model predictions of aerosol impacts
61 require understanding aerosol mixing states under different atmospheric conditions and
62 their effects on CCN activity (Ching et al., 2016; Zheng et al., 2021a). Current models
63 often oversimplify mixing states by assuming pure internal or external mixing (Winkler,
64 1973; Stevens et al., 2019; Riemer et al., 2019; Zheng et al., 2021b). This is problematic
65 because mixing states directly determine particle hygroscopicity distribution and CCN
66 estimates (Wang et al., 2010; Tao et al., 2024). For example, internal-mixed aerosol
67 particles have unimodal hygroscopicity distribution, while the external-mixed particles

68 are characterized by the bimodal/trimodal or partly overlapping structures (Spitieri et
69 al., 2023; Liu et al., 2025). Such simplifications can lead to significant errors, e.g.,
70 Sotiropoulou et al. (2007) found that mixing state assumptions caused two-fold N_{CCN}
71 estimation errors in global models.

72 Systematic observations across diverse environments are critical because aerosol
73 mixing states exhibit pronounced spatial-temporal variations (Ye et al., 2018; Hughes
74 et al., 2018; Liu et al., 2025). For example, continental and coastal regions present
75 contrasting scenarios (Ramachandran et al., 2016). The continental areas are dominated
76 by anthropogenic emissions, where aerosol aging is driven by industrial and traffic-
77 related pollutants (Huang et al., 2014; Ren et al., 2023). Particles here undergo
78 progressive internal mixing via photochemical process and heterogenous reactions,
79 altering their hygroscopic properties (Ervens et al., 2010; Tao et al., 2021). While the
80 coastal regions feature dynamic interactions between marine aerosols (e.g., sea salt) and
81 continental pollutants (Schill et al., 2015; Collins et al., 2013; Cheung et al., 2020).
82 Seasonal shifts in air mass sources (e.g., marine vs. continental dominance) might
83 create unique mixing state patterns (Xu et al., 2020, 2021a). For instance, summer
84 photochemical aging and heterogenous processes in coastal areas can enhance the
85 degree of internal mixing, while winter often retains more external mixing due to the
86 presence of the sea-salt particles with less-hygroscopic organic matter.

87 The continental aerosols influence regional cloud formation, while coastal
88 aerosols may provide insights into the characteristics of marine aerosols in region. The
89 properties of marine aerosols are significantly different from those of continental

90 aerosols, and therefore have distinct climate feedback mechanisms (Bellouin et al.,
91 2020; Xu et al., 2024; Liu et al., 2024). However, the current models lack regional-
92 specific mixing state parameters and usually assume uniform mixing in both
93 environments. This could lead to large uncertainties in predicting CCN concentrations,
94 highlighting the need for site-specific observations. For example, Ren et al. (2018)
95 found that the impact of aerosol mixing state on CCN activation characteristics ranged
96 from -34% to +16 % in urban atmosphere. Comparison between a fully internal mixture
97 assumption and using the mixing state index from the particle-resolved model, Ching
98 et al. (2017) found the obvious overestimation in CCN concentration estimation.
99 Especially in the regions eg., Amazon Basin, Central Africa and Indonesia, the particles
100 appeared to be more external, errors in CCN concentration would increase up to 100%
101 (Hughes et al., 2018). A detailed exploration of mixing state on CCN concentration in
102 global scale was conducted by Zheng et al. (2021a), and the results showed that the
103 mixing state varied spatially with more externally mixed over the North Atlantic Ocean,
104 off the coasts of Southern Africa, and Australia. Thus, assuming particles with
105 internally-mixed would introduce errors in CCN concentration of 50-100%.

106 Therefore, for quantifying the aerosol mixing state in the ambient atmosphere,
107 we apply the algorithm of entropy proposed by Riemer and West (2013) to investigate
108 the aerosol heterogeneity. This index has been applied to quantify the mixing state more
109 reasonably both in field campaigns (Zhao et al., 2021; Yuan et al., 2023) and model
110 simulations (Ching et al., 2016; Zheng et al., 2021a). However, most studies focused
111 on quantifying the particle heterogeneity in composition (Ching et al., 2019; Fierce et

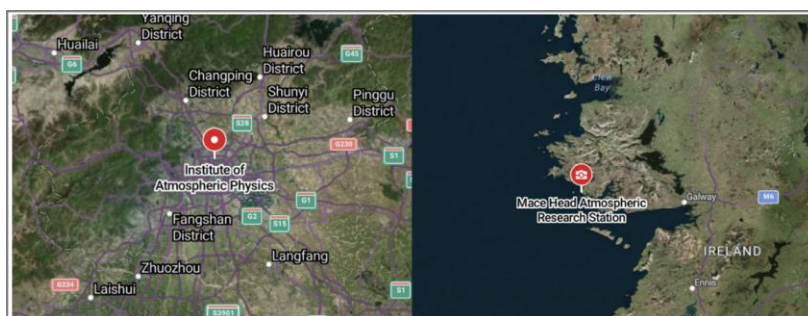
112 al., 2020; Zhao et al., 2021). Here we concentrated on evaluating the heterogeneity in
113 aerosol hygroscopicity for sub-micron particles, which directly related to CCN budget.
114 By refereeing to Yuan et al. 2023, the heterogeneity in hygroscopicity was investigated
115 by combining in-situ measurements of probability distribution function of the
116 hygroscopicity with the algorithm of entropy. Briefly, the mixing state index χ , is
117 devised based on the concept of information entropy concerning the distribution of
118 hygroscopicity across the aerosol population. It varies between 0 (external mixing
119 completely) and 1 (internal mixing completely). By integrating inland and coastal
120 measurements, this study will focus on addressing two key gaps, (1) How continental
121 vs. marine-dominated environments shape aerosol mixing states and CCN activity; (2)
122 Whether χ -based CCN parameterizations show regional dependencies, providing
123 critical constraints for climate models.

124 **2. Data and Methods**

125 **2.1 Field Campaigns**

126 The inland atmospheric measurements were conducted for two campaigns from
127 16 November to 6 December 2016 and 29 May to 13 June 2017 as a part of the Air
128 Pollution and Human Health (APHH) project (Shi et al., 2019), at the Institute of
129 Atmospheric Physics, Chinese Academy of Sciences (IAP, 39.97° N, 116.37° E) in
130 urban Beijing. The campaigns were complemented by the hygroscopicity and CCN
131 observations and were conducive to provide information on the aerosol hygroscopicity
132 affecting urban pollutions. This urban site exhibited highly variable aerosol populations

133 dominated by local anthropogenic sources including vehicular, cooking emissions, and
134 residential heating. Coastal measurements were performed at the Mace Head
135 atmospheric research station (MHD, 53.33° N, 9.90° W) from 1 November 2009 to 30
136 January 2010, and summer periods from 11 to 31 August 2009 and July 2010, which
137 located on the west coast of Ireland. Aerosol particles here experience alternating
138 influences from polluted continental and clean marine atmospheres. The map of the
139 sites was shown in Figure 1. More details about the campaigns were given in Fan et al.
140 (2020) and Xu et al. (2021a).



141
142 **Fig 1.** Map of the sites in the Inland of the Institute of Atmospheric Physics (IAP) and
143 Coastal of Mace Head (MHD). (© Google Maps, <https://maps.google.com/>, last access:
144 2 April 2025).

145 2.2 Instrumentation

146 Hygroscopicity measurements

147 The particle hygroscopicity at both sites was characterized using the humidified
148 tandem differential mobility analyzer (HTDMA). The hygroscopic growth factor (Gf),
149 defined as the ratio of the particle diameter at the fixed RH (90%) and dry diameter set

150 in this study for 40, 80, 110, 150, 200 nm at IAP and 35, 50, 75, 110 and 165 nm at
 151 MHD, respectively. [The RH calibration with ammonium sulfate for HTDMA system](#)
 152 [was given in Fig. S1](#). The Gf probability density function (Gf-PDF) was derived using
 153 the TDMAinv algorithm (Gysel et al., 2009). The number fraction (NF) of near-
 154 hydrophobic mode (NH: $Gf \leq 1.21$), and more hygroscopic mode (MH: $Gf > 1.21$) in
 155 IAP site was referred from Chen et al. (2022b). It was integrated into three modes for
 156 the MHD site with the near-hydrophobic mode (NH: $1 < Gf < 1.3$), more hygroscopic
 157 mode (MH: $1.3 \leq Gf < 1.85$) and sea salt mode (SS: $Gf \geq 1.85$) for further examination
 158 (Xu et al., 2021a).

159 Here for each particle size, the hygroscopicity parameter κ can be subsequently
 160 calculated using κ -Köhler theory (Petters and Kreidenweis, 2007):

$$161 \quad \kappa = (Gf^3 - 1) \cdot \left[\frac{1}{RH} \exp\left(\frac{4\sigma_{s/a}M_w}{RT\rho_w D_d Gf}\right) - 1 \right] \quad (1)$$

162 where RH is the HTDMA relative humidity (90% set in the instrument), $\sigma_{s/a}$ is the
 163 surface tension of pure water (0.072 mN m^{-1}), M_w and ρ_w are the molecular weight and
 164 the density of pure water, R is the gas constant, and T is the absolute temperature, D_d is
 165 the droplet diameter.

166 Then, the κ -PDF is obtained and normalized as $\int_0^\infty c(\kappa)d\kappa = 1$, where $c(\kappa)$ is
 167 normalized as κ -PDF. Further it was used to calculate the particle population
 168 heterogeneity (Calculation seen in Section 2.3).

169 [According to the \$\kappa\$ -Köhler theory, the critical diameter \(\$D_{cri}\$ \) corresponding to the](#)
 170 [supersaturation ratio can be expressed as:](#)

$$D_{crit} = \sqrt[3]{\frac{4A^3}{27\kappa \ln^2 S}}, A = \frac{4\sigma_s M_w}{RT\rho_w} \quad (2)$$

where S is the given supersaturation ratio (here 0.2% used in this study), κ is the mean value of the hygroscopicity parameter calculated in Equation (1).

Chemical components

For the inland atmospheric measurements, the non-refractory submicron aerosol (smaller than $1\mu\text{m}$, NR-PM₁) chemical composition was quantitatively characterized using the Aerodyne High-Resolution Time-of-Flight Aerosol Mass Spectrometer (HR-ToF-AMS) (DeCarlo et al., 2006), including sulfate (SO₄²⁻), nitrate (NO₃⁻), ammonium (NH₄⁺), chloride (Cl) and organics (Org). The black carbon (BC) mass concentration was determined from the light absorption with a seven-wavelength aethalometer (AE33, Magee Scientific Corp.).

Measurements of PM₁ in the coastal atmosphere were also performed by the HR-ToF-AMS, including major inorganic salts (non-sea-salt sulfate, nss-SO₄²⁻; methanesulfonic acid, MSA; NO₃⁻; NH₄⁺) and organic matter. The sea salt was quantified using NaCl ion signal, which has been demonstrated in previous studies (Ovadnevaite et al., 2014). The instrument operation and calibration have been described in previous studies (Ovadnevaite et al., 2014; Xu et al., 2019).

Aerosol number size distribution and CCN number concentration

Particle number size distributions (PNSD) were measured using an integrated system consisting of a Differential Mobility Analyzer (DMA; model 3081, TSI Inc.) coupled with a Condensation Particle Counter (CPC; model 3772, TSI Inc.). During the measurements at IAP, the PNSD covered the size range of 10-550 nm with a 5-minute

193 time resolution. It scanned size range of 20-500 nm at MHD with a 10-minute temporal
194 resolution. The CCN number concentrations were quantified at both sites using a
195 Droplet Measurement Technologies CCN counter (DMT-CCNc) (Lance et al., 2006).
196 The instrument's supersaturation (SS) settings were carefully calibrated before and after
197 each campaign using ammonium sulfate aerosol following Rose et al. (2008) (Fig. S1).
198 Four effective supersaturations (SS) were 0.14%, 0.23%, 0.40% and 0.76% at IAP site.
199 Four SS levels were 0.25%, 0.5%, 0.75% and 1% at MHD site with an uncertainty of
200 $\pm 0.03\%$. Using measurements at set supersaturation of 0.2% as an example explores the
201 CCN activity in the following discussions.

202 **2.3 Calculation the heterogeneity for aerosol particles**

203 To characterize the heterogeneous distribution of the hygroscopic and non-
204 hygroscopic components in populations (Chen et al., 2022b), we calculated the mixing
205 state index (χ) using the κ -PDF, following the methodology of Yuan et al. (2023). Two
206 surrogate groups in a population of N aerosol particles were assumed (Zheng et al.,
207 2021a). One surrogate group consists the non- and/or slightly hygroscopic species with
208 κ_N of < 0.05 and another group contains the more hygroscopic species with κ_H of 0.5-
209 0.6 (Yuan et al., 2023, referred inorganics). Ambient particles typically contain one or
210 two of the components and the κ lies between 0 and 0.6 at IAP or 0.8 at MHD as shown
211 in Figure S1S2. Taking into account the enhanced hydrophilicity of marine aerosols at
212 MHD site, calculation assuming κ_H values of 0.7 and 0.8 were shown in Fig.
213 S2S3. While these variations in κ_H introduced a mean uncertainty of 8% in χ values,

214 it did not significantly affect the seasonal or site comparisons. The volume fraction of
 215 two surrogate groups can be calculated based on the total κ according to the
 216 Zdanovskii–Stokes–Robinson (ZSR) mixing rule (Zdanovskii, 1948; Stokes et al.,
 217 1966).

218 The mixing state index χ is defined as the affine ratio of the average particle species
 219 diversity ($D\alpha$) and population species diversity ($D\gamma$) as:

$$220 \quad \chi = \frac{D\alpha - 1}{D\gamma - 1} \quad (23)$$

221 The average per-particle species diversity $D\alpha$ can be calculated as follows. First,
 222 the mixing entropies at bin i (H_i) are determined according to equation (34),

$$223 \quad H_i = -P_{i,N} \times \ln P_{i,N} - P_{i,H} \times \ln P_{i,H} \quad (34)$$

224 where $P_{i,N}$ and $P_{i,H}$ are the volume fraction of each group for the κ -PDF with X bins at
 225 bin i ($i=1,2,\dots,X$), and can be determined from the $P_{i,N} + P_{i,H} = 1$ and $P_{i,N} \times \kappa_N +$
 226 $P_{i,H} \times \kappa_H = \kappa_i$. Here $\kappa_N = 0.01$, $\kappa_H = 0.6$; κ_i represents the hygroscopicity parameter
 227 at bin i .

228 Based on the assumption that particles in the same diameter have the same mixing
 229 entropy $H_\alpha = \sum_{j=1}^N P_j \times H_j$, $P_j = \frac{V_j}{V_{total}} = \frac{1}{N}$; the per-particle mixing entropies H_α is
 230 determined according to equation (45),

$$231 \quad H_\alpha = \sum_{i=1}^X H_i \times c(\kappa)_i \times \Delta\kappa \quad (45)$$

232 where $c(\kappa)_i$ is the probability density of the normalized κ -PDF at bin i , and $\Delta\kappa$
 233 represents the bin width. Then, the average per-particle species diversity $D\alpha$ can be
 234 determined as $D\alpha = e^{H_\alpha}$;

235 The bulk population species diversity $D\gamma$ can be calculated as follows. First, the

236 aerosol population of the mixing entropy can be calculated as equation (56):

$$237 \quad H_\gamma = -P_N \times \ln P_N - P_H \times \ln P_H \quad (56)$$

238 where P_N and P_H are the volume fraction of the non-hygroscopic and hygroscopic
239 components in the population, and can be calculated by equation (67) and (78):

$$240 \quad P_N = \sum_{i=1}^X P_{i,N} \times c(\kappa)_i \times \Delta\kappa \quad (67)$$

$$241 \quad P_H = \sum_{i=1}^X P_{i,H} \times c(\kappa)_i \times \Delta\kappa \quad (78)$$

242 Then, the bulk population species diversity D_γ can be determined as $D_\gamma = e^{H_\gamma}$.

243 Here, the definition of surrogate species as supersets encompassing hygroscopicity
244 heterogeneity implies that the heterogeneity parameter χ ranges from 0 to 1. When the
245 mixing index χ approaches 0, it indicates a completely segregated state where
246 hygroscopic and non-hygroscopic species reside in distinct particles. While for the case
247 the mixing index χ to be 1 represents that the non-hygroscopic and hygroscopic species
248 distributing homogeneously throughout the aerosol population.

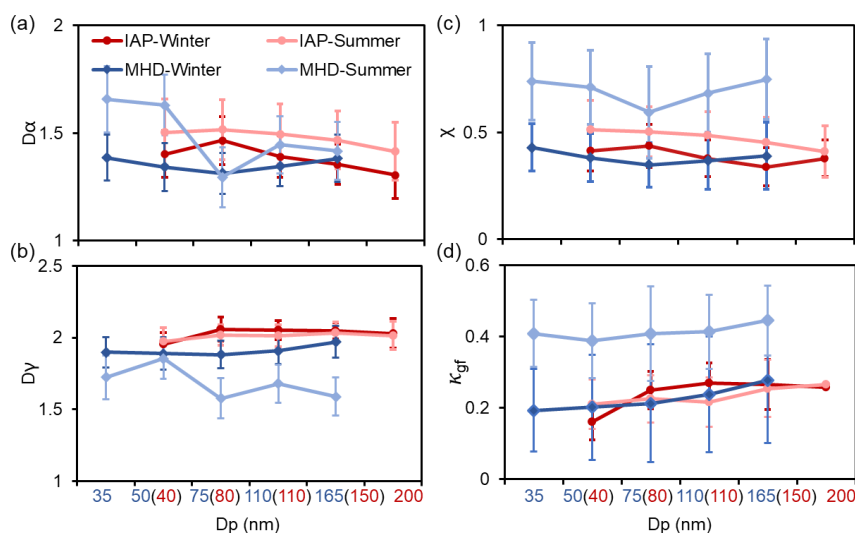
249 3. Result and Discussion

250 3.1 Comparison of the heterogeneity in the inland and coastal atmosphere

251 To characterize the hygroscopic heterogeneity of atmospheric aerosols, Figure 2
252 depicts variations in mixing state metrics ($D\alpha$, D_γ , χ) and the hygroscopic parameter
253 (κ_{gf}) across particle size distributions. The $D\alpha$ and χ decrease with increasing particle
254 diameter, accompanied by higher κ_{gf} values at IAP site. This trend indicates that inland
255 particle populations tend to homogenize into hygroscopic compositions through
256 primary particle aging or secondary formation processes (Liu et al., 2025; Chen et al.,

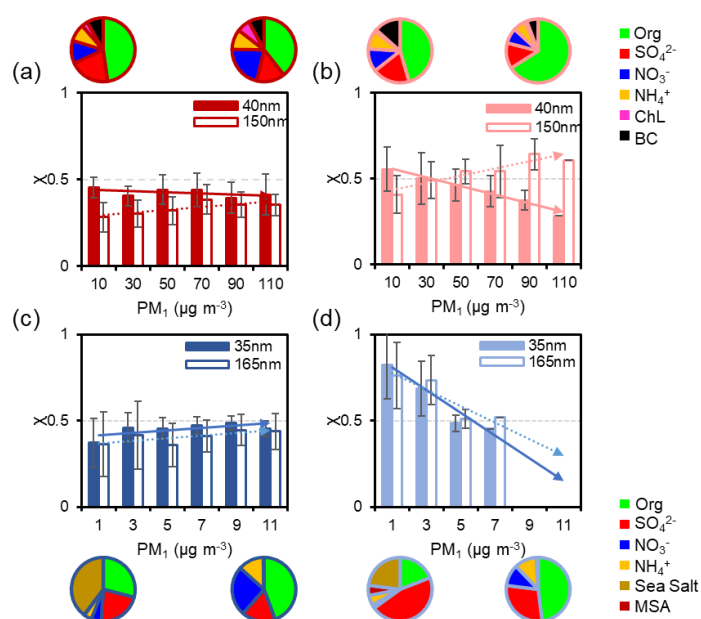
257 2022b; Zhong et al., 2022). In contrast, particles exhibit a non-monotonic pattern at
 258 MHD site: $D\alpha$ and χ decrease for Aitken-mode particles (<100 nm) but increase for
 259 accumulation-mode particles. The κ_{gf} shows consistent size-dependent increases in
 260 both winter and summer campaigns.

261 Notably, the mixing state metrics exhibit a pronounced minimum at 75 nm
 262 particles, influenced by distinct mechanisms: winter minima reflect the high sea salt
 263 fraction, while summer minima are driven by anthropogenic organic matter (Cheung et
 264 al., 2020; Xu et al., 2021a). Lower winter χ values—coupled with broader κ -PDF
 265 distributions—indicate stronger external mixing and compositional diversity compared
 266 to summer (Fig. S1S2). Seasonal χ and κ_{gf} disparities are more pronounced at MHD
 267 site, primarily driven by the seasonal alternation of marine and anthropogenic emission
 268 sources.



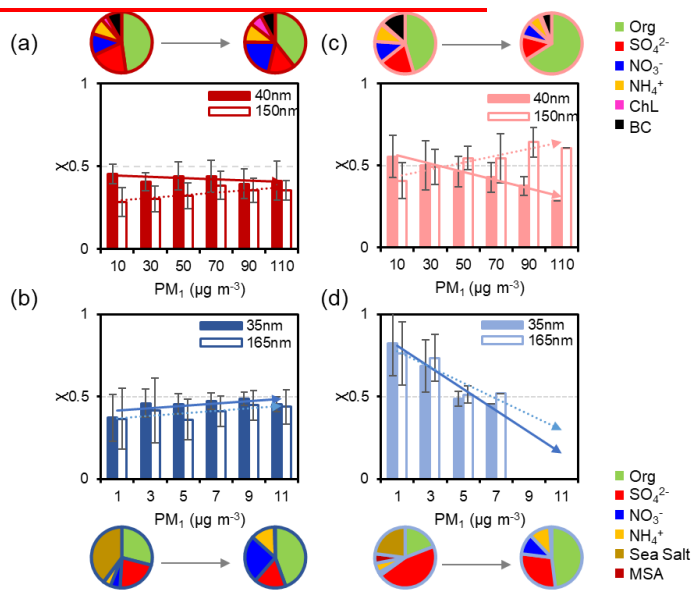
269
 270 **Fig 2.** Mean values of the $D\alpha$ (a), $D\gamma$ (b), χ (c) and κ_{gf} (d) for aerosols of five diameters
 271 during winter and summer periods at IAP and Mace Head sites.

272 Ultrafine particles (40 nm in IAP vs. 35 nm in MHD, Aitken mode) and larger
 273 particles (150 nm in IAP vs. 165 nm in MHD, accumulation mode) are selected to
 274 investigate distinct evolutionary processes of aerosol heterogeneity (Fig. 3 and Fig.
 275 [S3S4](#)). With the increasing of PM₁ concentration during winter, the variation in χ values
 276 exhibit only minor both at the IAP and MHD sites, generally fluctuating between
 277 approximately -0.04 and 0.08 (Fig. 3a and [b,c](#)). Inland accumulation-mode particles
 278 show a modest increase in χ , corresponding with a higher proportion of inorganic salts.
 279 Conversely, at MHD site, the composition fraction shifts from a sea-salt dominance



280
 281 **Fig 3.** Variation of the average χ for 40 nm and 150 nm particles at IAP and 35 nm and
 282 165 nm at MHD site with the particle mass concentration in IAP-winter (a), IAP-
 283 summer (b), MHD-winter (c) and MHD-summer (d). The pie charts represent the
 284 average mass fraction during four field measurements.

285 toward organic matter, accompanied by a ~20 % increase in nitrate content (Fig. 3b3c).
 286 In summer, the variation of χ with PM concentration becomes markedly pronounced at
 287 both IAP and MHD stations. For example, χ for 40 nm particles decreases as PM
 288 increases at IAP site (Fig. 3e3b). The elevated particle heterogeneity mainly arises from
 289 the locally primary emissions, corresponding to the enhanced primary organic
 290 emissions as shown in Fig. S4S5. It appeared more pronounced during evening rush
 291 hours. In contrast, χ for 150 nm particles increases from ~0.40 to ~0.60 with rising PM,
 292 reflecting enhanced secondary formation and internal mixing during pollution process
 293 that render the particle population more homogeneous. At coastal sites, χ declines with
 294 rising PM by approximately 0.37 for 35 nm particles and 0.24 for 165 nm particles,
 295 mirroring the shift in chemical composition makeup from inorganic dominance to
 296 greater organic content (Fig. 3d).



298 ~~Fig 3. Variation of the average χ for 40 nm and 150 nm particles at IAP and 35 nm and~~
299 ~~165 nm at MHD site with the particle mass concentration in IAP-winter (a), IAP-~~
300 ~~summer (b), MHD-winter (c) and MHD-summer (d). The pie charts represent the~~
301 ~~average mass fraction during four field measurements.~~

302 Diurnal variations of mixing state metrics ($D\alpha$, $D\gamma$, Gf-PDF and χ) at IAP and
303 MHD sites are shown in Figure 4. In IAP-winter, particles exhibited steeper declines in
304 $D\alpha$ and χ during evening rush hours than summer, indicating a higher fraction of non-
305 hygroscopic particles (40 nm) from fresh traffic emissions (Fig. 4a1 and S4S5).
306 Concurrently, reduced $D\gamma$ values suggest that the bulk population consists of uniformly
307 distributed less-hygroscopic (LH) components (Fig. 4c1). Aitken mode particles
308 showed bimodal and broader Gf-PDF distributions, corresponding to cooking activities
309 (11:00–13:00 LT) and traffic peaks (17:00–20:00 LT) (Cai et al., 2020). Midday
310 photochemical aging promoted more internally mixed aerosols (Yang et al., 2012; Liu
311 et al., 2025), as evidenced by increasing $D\alpha$ at the urban site (Fig. 4b1). Conversely, the
312 χ for accumulation-mode particles showed minimal diurnal variations both in IAP-
313 winter and IAP-summer. This is mainly due to the dominant hygroscopic mode for 150
314 nm particles (Fig. 4g4g1 and 4h1), especially during summer, which is mainly from
315 secondary formation or aging of the primary particles (such as the transformation from
316 primary organic aerosol (POA) to secondary organic aerosol (SOA) in Fig. S4S5)
317 (Wang et al., 2019; Fan et al., 2020).

带格式的: 段落间距段前: 0 磅

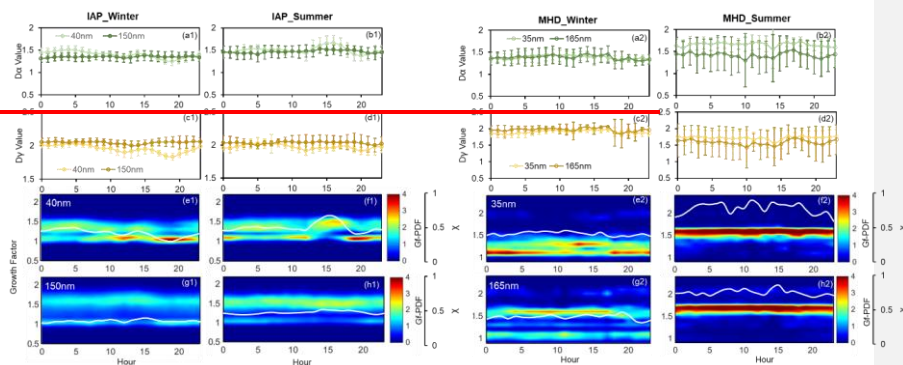
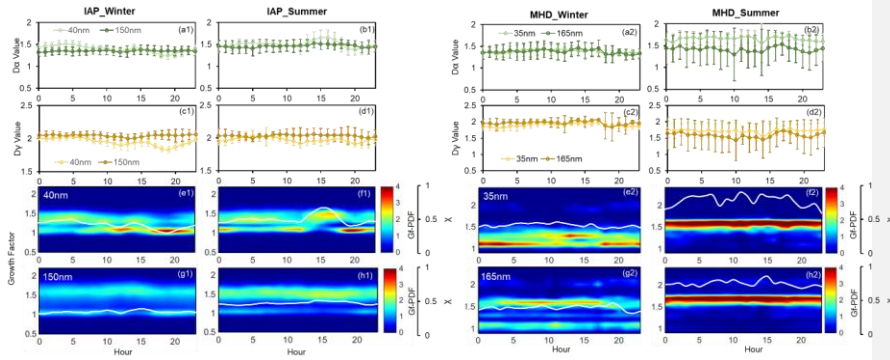


Fig. 4. Diurnal variation of $D\alpha$, $D\gamma$, Gf PDF, and χ during winter and summer periods for 40 nm and 150 nm aerosols at IAP (a1–h1) and for 35 nm and 165 nm aerosols at MHD site (a2–h2).

For the coastal atmosphere, the mixing state metrics ($D\alpha$, $D\gamma$, and χ) of Aitken and accumulation mode particles in winter exhibited analogous diurnal patterns, characterized by a descending trend at nightfall (Fig. 4a2–h2). This corresponds to an enhanced modal distribution of near-hydrophobic (NH) particles at 35 nm and more-hygroscopic (MH) particles at 165 nm. In summer, $D\alpha$ and $D\gamma$ both trended downward during daytime, with the decline of $D\gamma$ being more pronounced. A conspicuous seasonal discrepancy between Aitken and accumulation mode particles was observed in this region (Fig. 4a2–h2), where the mixing state index χ increased incrementally from winter to summer. Specifically, the mean χ for 35 nm particles escalated from 0.42 to 0.80, and for 165 nm particles, it rose from 0.39 to 0.76. This trend demonstrates a strong alignment with the spread factor (used as a measure of particle mixing state) documented by Xu et al. (2021a).

带格式的: 段落间距段前: 0 磅



334

335 **Fig 4. Diurnal variation of D_{α} , D_y , Gf-PDF, and χ during winter and summer periods**
 336 **for 40 nm and 150 nm aerosols at IAP (a1-h1) and for 35 nm and 165 nm aerosols MHD**
 337 **site (a2-h2).**

338 Similar to the mixing state χ , a very clear seasonal pattern of the aerosol
 339 hygroscopic distribution was found (Fig. 4e-h). In winter, the Gf-PDF diurnal profiles
 340 of both Aitken and accumulation mode particles showed bimodal distribution (Fig. 4e2-
 341 g2) as evident by the number fraction of nearly-hydrophobic and more hygroscopic
 342 modes (Fig. S5S6). The NH mode ~~was~~ likely ~~to be the~~ composed of anthropogenic
 343 organic matter and biogenic ~~origins~~ species derived from marine ~~mass~~ air masses (Xu et
 344 al., 2020), ~~especially for~~ this composition being particularly prominent in the
 345 Aitken mode. Additionally, Xu et al. (2021a) observed a higher abundance of the NH-
 346 mode in marine polar and Arctic air masses, this further supports the notion that NH
 347 particles are likely of biogenic origin, aside from contributions from anthropogenic
 348 activities. The more hygroscopic and sea salt mode was mostly contributed from the
 349 nss-sulfate and sea salt in winter (Xu et al., 2021a). Analogously, accumulation mode
 350 particles with a higher proportion of MH and SS mode (Fig. S5S6) primarily attributed

351 to the prevalence of non-sea-salt sulfate (nss-sulfate) and sea salt in the coastal
352 atmosphere (Xu et al., 2020). The bimodal and broad of hygroscopic distribution
353 suggested that particles were more diverse and external mixed, consistent with the
354 lower χ value in winter.

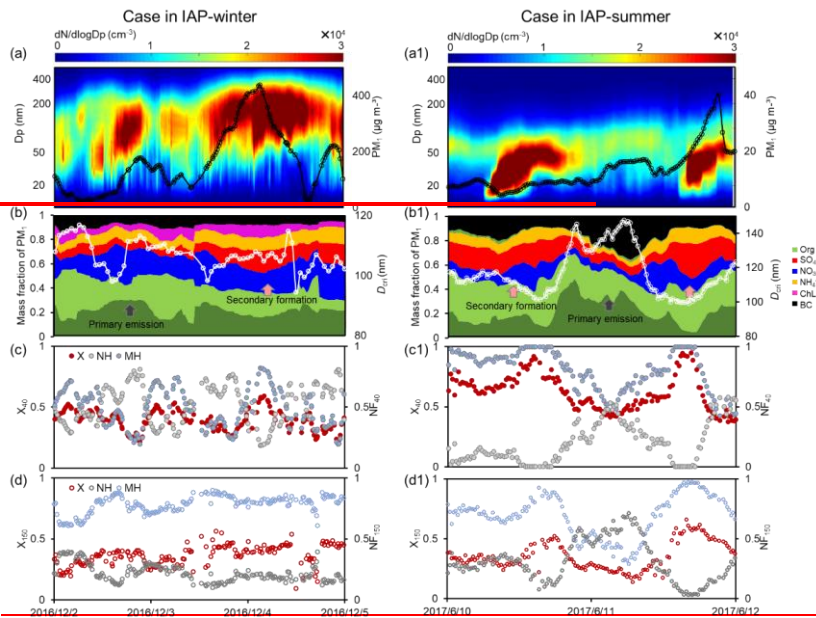
355 In contrast, summer observations revealed that Gf-PDFs of both Aitken and
356 accumulation mode particles transitioned to unimodal distributions, signifying particles
357 in summer had more homogeneous composition with a large extent of internal mixing
358 particles (with higher χ). Such diurnal trend in Gf-PDFs was consistent along with the
359 high number fraction of MH-mode and low NH-mode (Fig. S5S6). The higher
360 hygroscopicity and MH mode in summer were largely driven by the enhancement of
361 sulfate and decrease of organic matter (Fig. S5S6). And a clear shift from NH to MH
362 mode at midday might further demonstrate the promotion of photochemical aging in
363 summer (Xu et al., 2021a).

364 **3.2 Impacts of Primary Aerosol Emissions and Secondary Aerosol Formation on** 365 **Aerosol Mixing State**

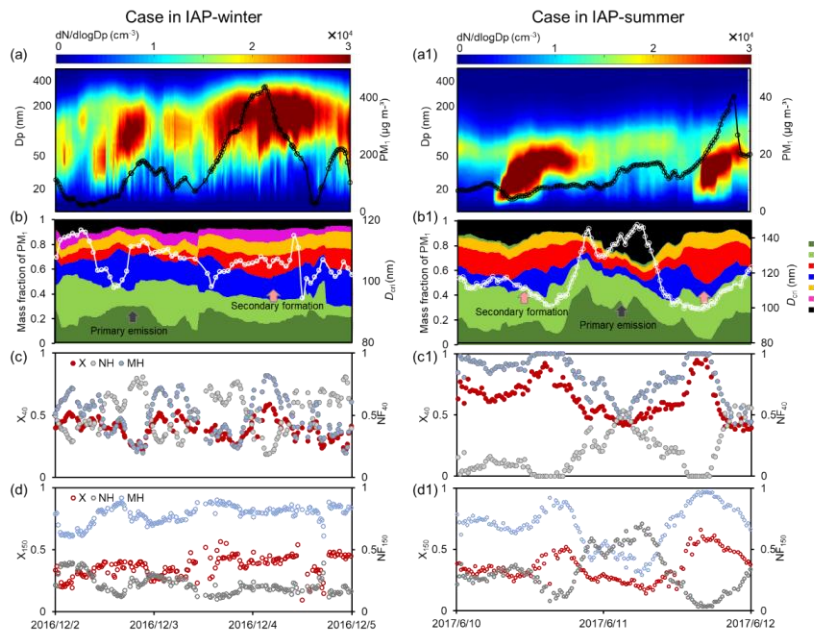
366 As already noted above, changes in χ were clearly associated with the chemical
367 composition varying with site and season. The relationships between the mixing state
368 index and the number fraction of hydrophobic and hygroscopic mode during four
369 campaigns are presented in Figure S6S7. The χ exhibited negative correlations with the
370 fraction of hydrophobic mode but a positive relationship with the fraction of
371 hygroscopic particles, highlighting the markedly different effects of the primary
372 emissions and secondary formation on aerosol mixing state (Tao et al., 2024). To gain

373 more insight on this effect between inland and coastal atmosphere, four case are
374 analyzed (Fig. 5 and 6): case for IAP-winter, case for IAP-summer, case for MHD-
375 winter and case for MHD-summer.

376 Case for IAP-winter is a heavy polluted event with the mean PM mass
377 concentration increased from 22 to 437 $\mu\text{g m}^{-3}$ (Fig. 5a-d). The 40- and 150-nm χ
378 patterns shifted quickly during the pollution periods. With the mass fraction of
379 hydrophobic compounds (ie., POA) in PM_{10} increased, the χ of 40-nm particles
380 decreased from 0.5 to 0.2, that is, an enhanced NH mode and a weaken MH mode (Fig.
381 5b-c). At this stage, large particles for 150 nm are mainly from aqueous formation with
382 more proportion of nitrate. The corresponding χ of 150 nm was higher. While with that
383 the mass fractions of secondary organic and inorganic compositions increased, particles
384 were more internal mixed with χ increased to be 0.6 for 40-nm and 0.53 for 150-nm
385 particles.



386

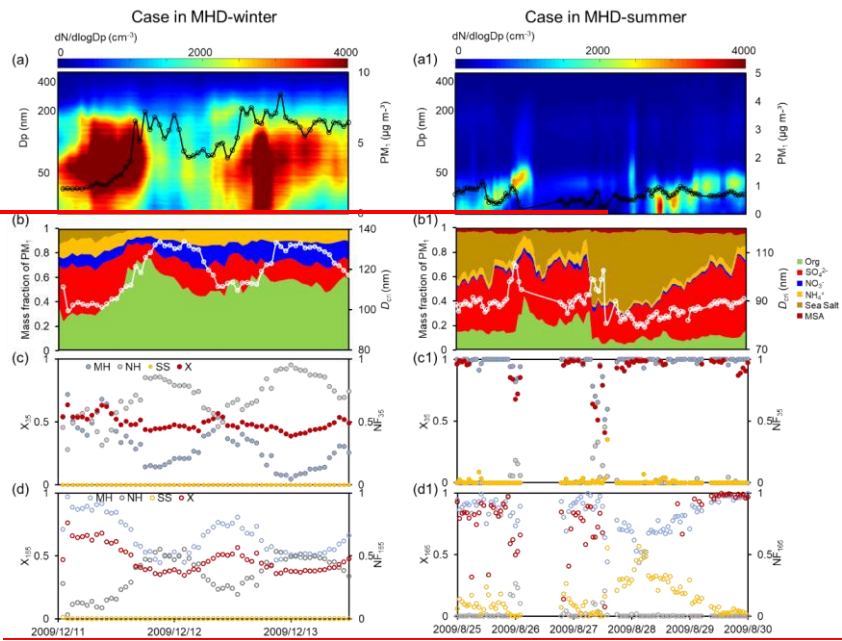


387

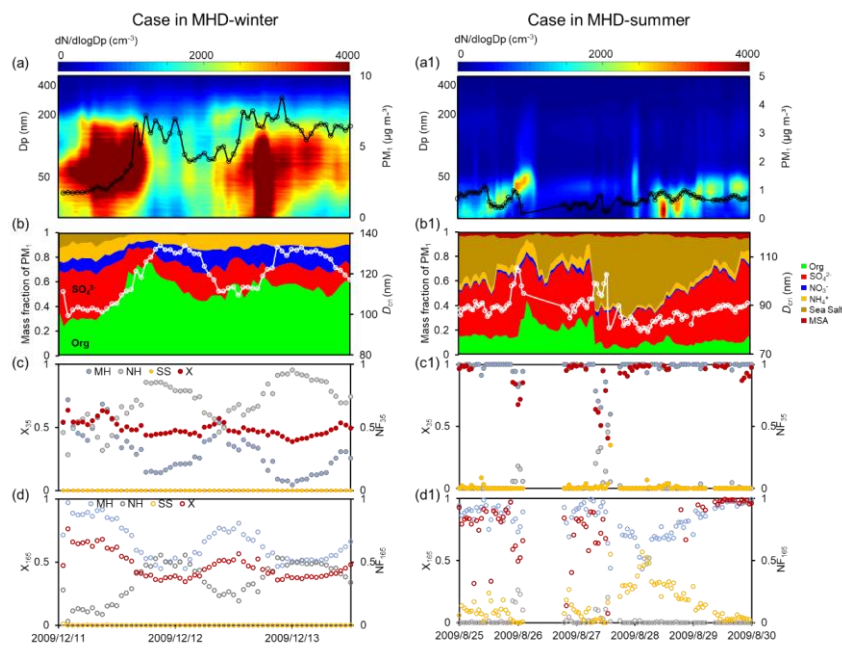
388 **Fig 5.** Case in IAP-winter (a-d) and IAP-summer (a1-d1). Particle number size
 389 distribution and PM₁ (a and a1), mass fraction of the PM₁ and the critical diameter (D_{crit})

390 (b [and b1](#)), mixing state index (χ), number fraction of the nearly hydrophobic mode
391 (NH) and more hygroscopic mode (MH) for 40 nm particles (c [and c1](#)), χ , NH and MH
392 for 150 nm particles (d [and d1](#)).

393 Case for IAP-summer is the typical new particle formation events (NPF) with the
394 mean PM_{10} of $13 \mu\text{g m}^{-3}$ (Fig. 5a1-d1). With the evolution of NPF events, the χ of 40-
395 and 150-nm particles increased to be 0.95 and 0.61 with the enhanced proportion of
396 more-hygroscopic components (ie., SOA, NO_3^- , SO_4^{2-}). The χ pattern is opposite of that
397 the number fraction of NH mode and consistent with the variation of MH mode (Fig.
398 [S6S7](#)). Note that a sudden decrease in χ on June 11th was disturbed by the strong
399 primary emission. The chemical mass fractions showed more POA and black carbon
400 with an enhanced NH mode and a weaker MH mode (Fig. 5b1-d1). The χ of 40-nm
401 particles decreased to be 0.4 and that of the 150-nm particles decreased to be 0.2. The
402 χ patterns appear to similar transitions for Aitken and accumulation-mode particles
403 during haze and NPF events. The increase in χ is synchronous with the increase in MH
404 mode from secondary formation but opposite with that of LH mode from primary
405 emissions. This implies that the primary emissions would lead particles more external
406 mixing while secondary formation would promote aerosol more internal mixed in
407 Inland atmosphere.



408



409

410 **Fig 6.** Case in MHD-winter (a-d) and MHD-summer (a1-d1). Particle number size

411 distribution and PM_{10} (a [and a1](#)), mass fraction of the PM_{10} and the critical diameter
412 (D_{crit}) (b [and b1](#)), mixing state index (χ), number fraction of the nearly hydrophobic
413 mode (NH) and more hygroscopic mode (MH) for 35 nm particles (c [and c1](#)), χ , NH
414 and MH for 165 nm particles (d [and d1](#)).

415 Case for MHD-winter is a high organic matter pollution event with the mean PM_{10}
416 of $5.2 \mu\text{g m}^{-3}$ and 52% mass fraction of organics (Fig. 6a-d). Larger presence of
417 anthropogenic organic matter resulted the NH mode for 35-nm particles to be 95% and
418 165-nm particles to be 53% (Fig. 6). The χ of 35- and 165-nm particles decreased with
419 the NH mode increased (Fig. [S6S7](#)), similar with the case for IAP site. There was a
420 steady increase in χ when the MH-mode particles started increasing with the increase
421 in mass fraction inorganics, eg., 35 nm particles showed the mean χ increasing from
422 0.43 to 0.57 and 165 nm particles from 0.35 to 0.6. This indicated that the trend of
423 aerosol mixing state closely followed the evolution emission and secondary formation.

424 Case for MHD-summer is an extremely clean event with the mean PM_{10} of $0.7 \mu\text{g}$
425 m^{-3} (Fig. 6a1-d1). The dominated MH mode was found throughout the case, which
426 could be attributed from the high mass fraction of nss-sulfate (41% average). Compared
427 with the case in MHD-winter, the mean proportion of organic has decreased to be 15%.
428 Therefore, the χ remains at a high value (mean χ of 0.9 for 35-nm and 0.8 for 165-nm
429 particles). Until August 28th, a stronger increase in the mass fraction of sea salt and
430 accordingly SS mode in larger-size particles was observed. The χ decreased rapidly
431 with the decrease in MH mode and enhanced SS mode, especially for the accumulation
432 mode particles, suggesting the sea spray production makes particles more externally

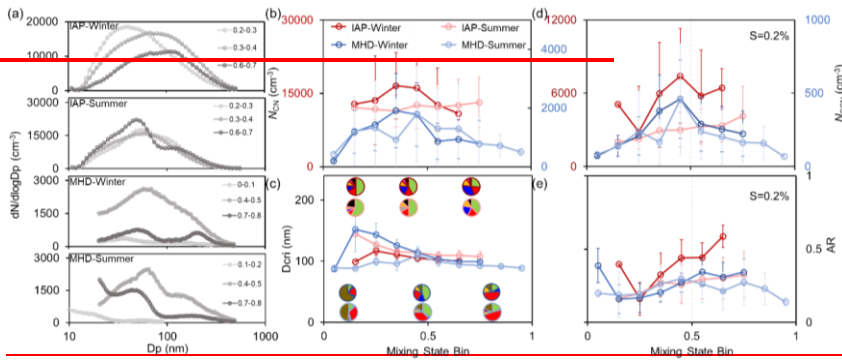
433 mixed.

434 In summary, these results suggest that the primary emission and secondary
435 formation drive the hygroscopic distribution and can result in significant variation of
436 aerosol mixing state χ both in Inland and coastal atmosphere. The pattern of χ varied
437 among site and season, highlighting the importance of considering the impact of mixing
438 state on CCN activity.

439 3.3 Impact of Covariation relationships between the Mixing State and CCN 440 Activity

441 The mixing state of particle populations undergoes dynamic transformations
442 during atmospheric aging, profoundly influencing their CCN activity. Unlike prior
443 CCN closure studies that assumed mixing states based on chemical component
444 fractions (Yang et al., 2012; Padró et al., 2012; Ren et al., 2018), this work employs the
445 hygroscopicity distribution- and entropy-derived mixing state index χ , which quantifies
446 to clarify the distribution covariation relationships between the mixing state and CCN
447 activity. Given that CCN activity reflects the characteristics of hygroscopic and non-
448 hygroscopic species (Zheng et al., 2021a; Ching et al., 2017), the entire particle
449 population while χ is calculated from HTDMA measurements at specific particle
450 diameters, this study chooses the N_{CCN} , activation ratio (AR) at supersaturation of 0.2%
451 and the mean χ for accumulation-mode to illustrate the covariation characteristic
452 approximately. This approach is employed to ensure that both variables/parameters
453 reflect the characteristics of the accumulation-mode particle population. The
454 variations covariations of particle size and chemical composition with the increments of

455 mixing state (χ) (ranging from 0 to 1 with the step intervals of 0.1) are illustrated in
 456 Figure 7, presenting. This figure provides key insights e~~f~~into two fundamental
 457 determinants of CCN activity (Dusek et al., 2006).-



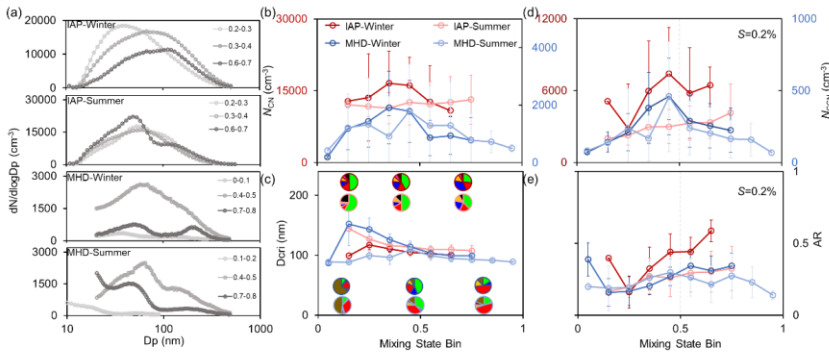
458 **Fig. 7. Comparison of the average particle number size distribution (PNSD) in different**
 459 **mixing state index (χ) (a), CN number concentration (N_{CN}) as a function of χ (b),**
 460 **Critical diameter (D_{crit}) at $S=0.2\%$ and mass fraction of chemical composition as a**
 461 **function of χ (c), CCN number concentration (N_{CCN}) (d) and activation ratio (AR) at**
 462 **$S=0.2\%$ a function of χ (e).**

464 As χ increases, the peak diameter (D_{peak}) of the particle number size distribution*
 465 (PNSD) shifts toward larger sizes (Fig. 7a and Fig. S7S8), while peak concentrations
 466 occur within the intermediate χ range (0.3–0.6). This trend indicates that CN number
 467 concentration (N_{CN}) first increases, driven by primary emissions and new particle
 468 formation, then decreases due to mixing and aging processes (Fig. 7b). Notably, new
 469 particle formation events frequently occurred in IAP-summer (Fig. S8S9),
 470 corresponding the gradually increase of χ . And the χ for Aitken-mode is significantly
 471 larger than the accumulation-mode particles during this period. Thus, N_{CN} exhibits a

设置了格式: 字体: Times New Roman, 小四

带格式的: 段落间距段前: 0 磅

472 sustained slight increase as the degree of the internal mixing increases in IAP-summer.



473
474 **Fig 7. Comparison of the average particle number size distribution (PNSD) in different**
475 **mixing state index (γ) (a), CN number concentration (N_{CN}) as a function of γ (b),**
476 **Critical diameter (D_{crit}) at $S=0.2\%$ and mass fraction of chemical composition as a**
477 **function of γ (c), CCN number concentration (N_{CCN}) (d) and activation ratio (AR) at**
478 **$S=0.2\%$ a function of γ (e).**

479 The critical diameter (D_{crit})—defined as the minimum size required for activation
480 at a given supersaturation—depends on aerosol hygroscopicity. ThisIn turn, this
481 hygroscopicity is jointly determined by both the hygroscopicity and the mass fraction
482 of individual soluble components and their mass fractions in the aerosol (Petters and
483 Kreidenweis, 2007). Using measurements at supersaturation of 0.2% as an example,
484 Fig. 7c shows that D_{crit} decreases with increasing highly hygroscopic inorganic
485 components (e.g., sulfate, nitrate) in the inland atmosphere. In contrast, coastal D_{crit}
486 exhibits nonlinear variations with γ : high external mixing (low γ) elevates D_{crit} due to
487 dominant organic components, reducing sea salt particle fractions. As γ increases, the
488 mass fraction of non-sea-salt sulfate (nss-sulfate) rises, enhancing activation potential

设置了格式: 字体: Times New Roman, 小四

带格式的: 段落间距段前: 1 行

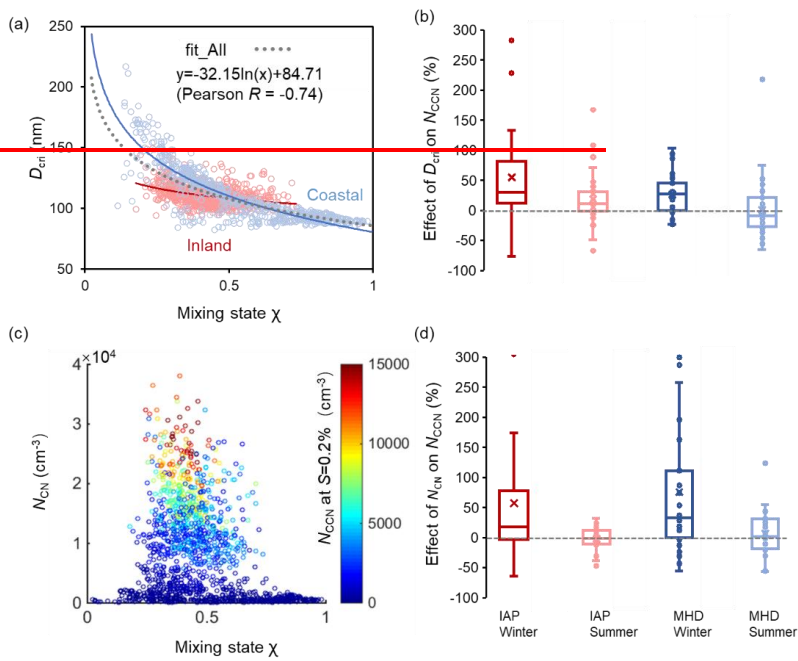
489 by decreasing D_{cri} .

490 The ~~dependence~~covariation characteristic of CCN activity at 0.2% supersaturation
491 ~~on~~with mixing state index χ reveals distinct inter-atmospheric differences, as shown in
492 Fig. 7d-e. In ~~the inland atmosphere~~IAP, N_{CCN} at $S=0.2\%$ demonstrates a monotonic
493 increasing trend with χ , attributed to the synergistic effects of rising N_{CN} and decreasing
494 D_{cri} (Fig. ~~S9S10~~S9S10). By contrast, coastal N_{CCN} follows a pattern analogous to N_{CN} , with
495 peak concentrations shifting toward higher χ values. This highlights the dominant role
496 of particle size effects in enhancing CCN concentrations under marine-influenced
497 conditions (Dusek et al., 2006).

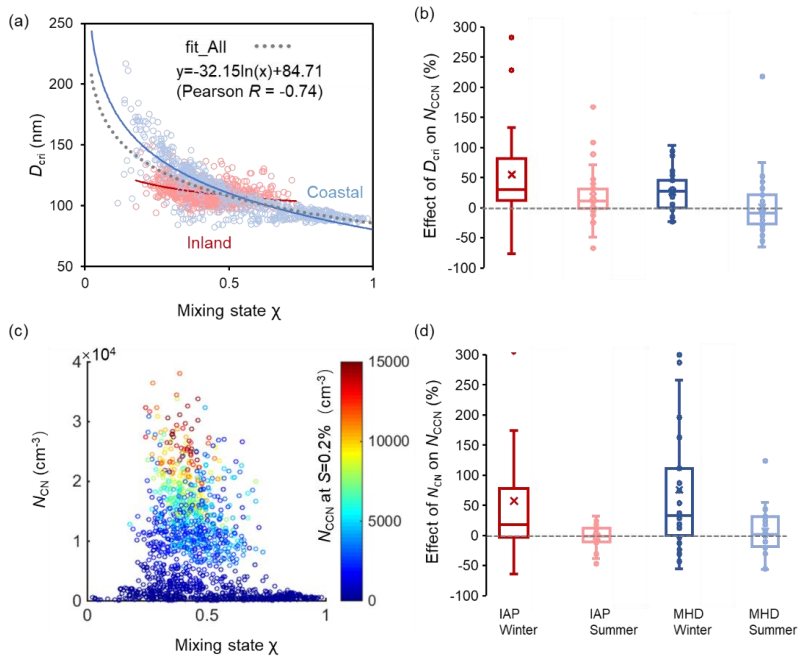
498 Two distinct $D_{\text{cri}}-\chi$ trends underpin these disparities: one remains stable, driven by
499 the inherent hygroscopicity of sea salt, while the other exhibits steep D_{cri} declines
500 associated with anthropogenic pollution as internal mixing intensifies. These
501 discrepancies are further manifested in the nonlinear $D_{\text{cri}}-\chi$ relationship. The activation
502 ratio (AR)—quantifying aerosol cloud droplet formation potential at fixed
503 supersaturation—also varies by site (Fig. 7e). Notably, AR shows a marked increase
504 with χ in IAP-winter, likely due to enhanced N_{CCN} from the elevated inorganic fraction
505 under higher mixing states (Fig. 3). Conversely, the inorganic fraction decreases during
506 other sampling periods, dampening AR growth.

507 ~~To better interpret the impact of mixing state on CCN concentrations, Fig. 8~~
508 ~~quantifies the relative change in N_{CCN} at $S=0.2\%$ as mixing state index χ increases,~~
509 ~~contextualizing how CN concentration and chemical compositions (i.e., D_{cri}) evolve~~
510 ~~with mixing and aging across particle populations. D_{cri} demonstrates heightened~~

511 sensitivity to minor χ fluctuations at low mixing states ($\chi < 0.5$; Fig. 8a), whereas further
 512 increases in internal mixing (higher χ) exert negligible influence on D_{crit} for already
 513 internally mixed particles. This behavior suggests that the D_{crit} - χ relationship may
 514 enable a novel parameterization for D_{crit} estimation, a framework that is not yet reported
 515 in prior literature.



516
 517 **Fig. 8.** Dependency of the critical diameter (D_{crit}) on



518
 519 **Fig 8.** Covariation characteristics of the critical diameter (D_{cri}) with the χ (a), relative
 520 change of CCN number concentration (N_{CCN}) at supersaturation $S = 0.2\%$ with the
 521 reduction in D_{cri} (b); ~~Dependency~~ Covariation characteristics of the CN number
 522 concentration (N_{CN}) ~~on~~ with the χ , different colors represent the N_{CCN} (c), relative
 523 change of N_{CCN} with the change in N_{CN} (d).

524 Fig. 8 further shows the covariation characteristics of CN concentration, chemical
 525 compositions (i.e., D_{cri}) with mixing state across particle populations. D_{cri} exhibits
 526 heightened sensitivity to minor χ fluctuations in the mixing state (χ) when $\chi < 0.5$ (Fig.
 527 8a). In contrast, for particles already characterized by internal mixing, further increases
 528 in χ (i.e., higher degrees of internal mixing) exert a negligible influence on D_{cri} . This
 529 behavior pattern implies that the D_{cri} - χ relationship could enable a novel

530 parameterization for D_{cri} estimation, a framework that has not yet been reported in the
531 existing literature.

532 Aerosol ~~data points~~observation at MHD site (blue dots) span a broad D_{cri} range
533 (80–220 nm) with χ varying from 0.1 to 1, reflecting alternating influences of highly
534 hygroscopic inorganic salts (sea salt, sulfate) and less-hygroscopic organic matter. In
535 contrast, aerosols—dominated by anthropogenic pollutants—exhibit a narrower D_{cri}
536 range (90–150 nm) at IAP site. Both environments show negative D_{cri} - χ correlations,
537 but with distinct functional forms: MHD aerosols feature an exceptional logarithmic fit
538 ($D_{\text{cri}} = -42.98\ln(\chi) + 80.36$, $R^2 = 0.75$; Fig. 8a blue line), while IAP aerosols (red line)
539 yield a shallower slope (-12.04). Pooling all data, we derive a generalized
540 parameterization: $D_{\text{cri}} = -32.15\ln(\chi) + 84.71$ (Pearson $r = -0.74$, $R^2 = 0.54$). As ~~already~~
541 discussed above, strong impact of primary emission and secondary formation on
542 aerosol mixing state was observed in both sites (Fig. 5 and 6). ~~It also provides even~~One
543 could obtain more details on the D_{cri} - χ correlations. For example, the D_{cri} exhibited
544 rapidly ~~increased~~increase with the increase of primary emissions (ie., mass fraction of
545 POA enhanced) during polluted periods. The D_{cri} pattern appeared opposite with that of
546 the mixing state index, especially for the accumulation-mode particles. More
547 pronounced D_{cri} - χ correlations were observed during the new particle formation (Fig.
548 5a1-d1). The decreasing presence of D_{cri} matched the increasing proportion of SO_4^{2-}
549 and SOA with the χ increased during NPF events. Similar correlations between the
550 critical diameter and mixing state index were also found in the coastal atmosphere,
551 especially for the case of the enhanced anthropogenic organic matter and sea salt

552 production (Fig. 6). This implies that the relationship between the D_{cri} and χ might be
553 disturbed by the variation of emission pollution and secondary formation processes,
554 resulting in spatiotemporal differences. The D_{cri} reduces by 2.2–6.8% with the mixing
555 state increase at a step of 0.1, with the steepest winter decline (Fig. S11).

556 ~~Box plot analyses (Fig. S10) show that the mixing state reduces D_{cri} by 2.2–6.8%~~
557 ~~across campaigns, with the steepest winter decline.~~ Changes in N_{CN} with differ starkly
558 between environments: positive effects in polluted inland air (+9%) versus negative
559 effects in coastal regions (-2%). Aerosols in IAP, frequently perturbed by primary
560 emissions and new particle formation, exhibit elevated N_{CN} (peaking at $\chi = 0.2$ – 0.7),
561 while in MHD N_{CN} remains $\sim 5000 \text{ cm}^{-3}$ across all χ .

562 ~~To isolate the impacts of critical diameter (D_{cri}) and condensation nuclei number~~
563 ~~concentration (N_{CN}) on CCN concentration, we We categorized data into two groups:~~
564 C1 (particles within specific N_{CN} ranges) evaluates N_{CCN} ~~variations~~ covariations mainly
565 driven by D_{cri} - χ relationships, while C2 (particles within fixed D_{cri} intervals) assesses
566 N_{CN} - χ effects (Fig. 8b). Relative changes (RC) in D_{cri} , N_{CN} , and N_{CCN} with χ were
567 calculated by comparing successive χ increments (χ_{i+1} vs. χ_i , $i=0,0.1\dots 1$) within
568 defined N_{CN} ~~or~~ D_{cri} windows.

569 Notably, ~~change in N_{CCN}~~ the covariation relationship between the N_{CCN} and mixing
570 state exerts more pronounced ~~effects on~~ for the case of externally mixed aerosols
571 dominated. For example, MHD-winter aerosols (high external mixing; $\chi_{\text{mean}}=0.38\pm 0.12$)
572 showed RCs in N_{CCN} ~~RCs~~ of 23% (C1) and 72% (C2), whereas MHD-summer aerosols
573 (high internal mixing; $\chi_{\text{mean}}=0.69\pm 0.19$) exhibited negligible effects (-2.5% in C1, 0.9%

带格式的: 缩进: 首行缩进: 3 字符

574 in C2). Inland atmospheres, despite smaller seasonal χ variations, showed analogous
575 trends: RCs of N_{CCN} in winter ~~N_{CCN} RCs~~ (55% in C1, 57% in C2 for external mixing)
576 exceeded summer values for more internally mixed populations (Fig. 8d). These results
577 confirm that hygroscopic heterogeneity strongly influences N_{CCN} under external mixing,
578 aligning with prior work (Ching et al., 2017).

579 ~~With the variation in mixing state index χ , changes in N_{CCN}~~ The covariation
580 characteristics are most pronounced during winter in both environments, attributed to
581 heightened winter D_{crit} sensitivity to χ : a 0.1 χ increase reduces D_{crit} by 5.2% (winter),
582 boosting N_{CCN} by 39%, versus 2.4% D_{crit} reduction (summer) yielding only 6% N_{CCN}
583 enhancement. Concomitantly, winter N_{CN} - χ effects on N_{CCN} reach 65%, far exceeding
584 summer responses.

585 ~~Contrasting with prior~~In contrast to previous evaluation methods that oversimplify
586 mixing states (Ren et al., 2018; Xu et al., 2021b), the entropy-based framework ~~adopted~~
587 ~~herein enables explicit quantification of~~employed in this study explicitly characterizes
588 the covariation between the CCN activity ~~evolution and transitions~~ in ~~response to the~~
589 mixing state ~~transitions~~. Aerosols in IAP-winter are presumably shaped by intense
590 urban pollution sources—including traffic emissions, residential heating, and cooking
591 activities—thereby enriching the externally mixed particle fraction (Fan et al., 2020;
592 Xie et al., 2020). Analogously, aerosols in MHD-winter exhibit dominant external
593 mixing, consisting of near-hydrophobic and hydrophilic particle mixtures (Xu et al.,
594 2021a). As illustrated in Fig. ~~S1, S2, the~~ winter aerosol ~~populations display~~population
595 exhibits bimodal or multimodal κ -PDF distributions, ~~evidencing this pattern~~

596 indicates a high-degree of external mixing, with the aerosols characterized by
597 chemically diverse compositions. TheseCollectively, these results collectively
598 highlightunderscore the pivotal role of mixing state heterogeneity in modulating CCN
599 activity across different environments.

600 4. Conclusions

601 The mixing state of aerosol populations undergoes complex transformations
602 during atmospheric aging, altering the distribution of hygroscopic and non-hygroscopic
603 components and thus influencing CCN activity (Xu et al., 2021a; Ching et al., 2017).
604 This study derived a mixing state index (χ) from field-measured hygroscopicity
605 distributions, systematically investigating its impacts on the covariation relationship
606 between the mixing state and CCN activity at two inland and coastal environments.
607 Results provide field evidence that aerosol mixing states generally reside between
608 purely internal and external extremes (Chen et al., 2022b). Aerosol mixing state is
609 largely influenced by the primary emissions and secondary formation process.
610 Externally-mixed particles with more hydrophobic-mode originate chiefly from
611 primary emissions in IAP, while that of more sea-salt mode from sea spray in MHD.
612 While it becomes more internally-mixed as the enhanced fraction of more-hygroscopic
613 mode and decreased of hydrophobic mode during the aging process. This highlights a
614 dual regulatory mechanism of mixing state and its potential impact on hygroscopic
615 distribution and CCN activity.

616 As χ increases, CN number concentrations (N_{CN}) first rise—driven by primary
617 emissions and new particle formation—then decline due to condensation and

618 coagulation during aging. Additionally, a logarithmic decreasing relationship between
619 critical diameter (D_{cri}) and χ was identified for both inland and coastal particles,
620 parameterized as $D_{\text{cri}} = -32.15\ln(\chi) + 84.71$ (Pearson $R = -0.74$, $R^2 = 0.54$). This offers
621 a practical approach to estimate D_{cri} from χ , serving as a general framework for
622 integrating mixing state effects on CCN activity in atmospheric models.

623 Entropy-based analyses ~~confirm further support~~ the ~~pivotal role of covariation~~
624 ~~relationships between the~~ mixing state ~~in regulating and~~ N_{CCN} , especially for externally
625 mixed aerosols: ~~a 0.1 χ increase can enhance N_{CCN} by 39–65%.~~ Current models often
626 oversimplify aerosol mixing states as purely internal or external (Stevens et al., 2019;
627 Bauer et al., 2013), the latter being particularly sensitive to organic matter (Ren et al.,
628 2018; Bhattu et al., 2015). Such simplifications introduce significant biases in N_{CCN}
629 estimation (Riemer et al., 2019; Ching et al., 2019). The χ - D_{cri} parameterization
630 proposed here offers a novel approach to reduce model complexity in representing
631 aerosol hygroscopicity and CCN activation, enabling more accurate simulations of
632 aerosol CCN capacity. It is expected mitigate the underestimation in CCN compared
633 with the complete external mixing assumption, while effectively alleviates the
634 overestimation that arises from applying the complete internal mixing assumption in
635 regions characterized by high external mixing (Zheng et al., 2021a). This advancement
636 improves our understanding of aerosol-cloud interactions (IPCC, 2021; Rosenfeld et al.,
637 2019), critical for refining climate effect assessments.

638 **Data availability**

639 All data used in the study are available at <https://doi.org/10.3974/geodb.2019.06.11.V1>

640 (Fan et al., 2019) and <http://doi.org/10.17632/3dx6pnx869.1> (Xu et al., 2021a).

641 **Author contributions**

642 RH and JR conceived the conceptual development of the paper. JR, FZ and WX directed
643 and performed the experiments with YW and LC. FZ and YS provided the dataset in
644 the inland site. JO, DC and CO provided the dataset in the coastal site. JR conducted
645 the data analysis and wrote the draft. All authors edited and commented on the various
646 sections of the paper.

647 **Competing interests**

648 The contact author has declared that none of the authors has any competing interests.

649 **Supporting Information**

650 Additional analysis results that were applied in this study. ~~Mean~~[Example of](#)
651 [calibration results of HTDMA and CCN used in this study \(Figure S1\)](#), [mean](#) values of
652 the κ -PDF for aerosols of five diameters (Figure [S1S2](#)), sensitivity of the hygroscopic
653 parameter for the group of the hygroscopic species on the mixing state index χ (Figure
654 [S2S3](#)), time series of the average per-particle species diversity $D\alpha$, the bulk population
655 species diversity $D\gamma$, and their affine ratio χ (Figure [S3S4](#)), diurnal trend of particle size,
656 chemical mass fraction and number fraction (NF) of hydrophobic and hygroscopic
657 mode in IAP (Figure [S4S5](#)) and in MHD (Figure [S5S6](#)), mixing state as a function of
658 number fraction of hydrophobic and hygroscopic mode (Figure [S6S7](#)), variation of the
659 peak diameter (D_{peak}) with the mixing state index (Figure [S7S8](#)), particle number size
660 distribution and mixing state during new particle formation events (Figure [S8S9](#)),

661 diurnal variation of χ and CN concentration during winter and summer periods for 40
662 nm and 150 nm aerosols in inland and for 35 nm and 165 nm aerosols in coastal site
663 (Figure [S9S10](#)), relative change of the critical diameter and CN concentration with the
664 mixing state index χ (Figure [S10S11](#)) (PDF).

665 **Acknowledgements**

666 This work was funded by the National Natural Science Foundation of China (NSFC)
667 under Grant No. 42525301, 42405118 and 42475112, the State Key Laboratory of
668 Loess Science, Institute of Earth Environment, Chinese Academy of Sciences
669 (SKLLQG2429), the Guangdong Natural Science Foundation (Grant No.
670 2024A1515011005). We thank all participants of the field campaign for their hard work
671 and sharing of the data.

672 **References**

- 673 Bhattu, D., Tripathi, S. N.: CCN closure study: Effects of aerosol chemical composition
674 and mixing state, *Journal of Geophysical Research: Atmospheres.*, 120(2), 766–
675 783, <https://doi.org/10.1002/2014JD021978>, 2015.
- 676 Bellouin, N., Quaas, J., Gryspeerdt, E., Kinne, S., Stier, P., Watson-Parris, D., Boucher,
677 O., Carslaw, K. S., Christensen, M., Daniau, A-L., Dufresne, J.-L., Feingold, G.,
678 Fiedler, S., Foster, P., Gettelman, A., Haywood, J. M., Lohmann, U., Malavelle, F.,
679 Mauritsen, T., McCoy, D. T., Schulz, M., Schwartz, S. E., Sourdeval, O.,
680 Storelvmo, T., Toll, V., Winker, D., and Stevens, B: Bounding global aerosol
681 radiative forcing of climate change, *Rev. Geophys.*, 58, e2019RG000660,
682 <https://doi.org/10.1029/2019RG000660>, 2020.
- 683 Bauer, S. E., Ault, A., Prather, K. A.: Evaluation of aerosol mixing state classes in the
684 GISS modelE-MATRIX climate model using single-particle mass spectrometry

685 measurements, *Journal of Geophysical Research: Atmospheres.*, 118, 9834–9844,
686 <https://doi.org/10.1002/jgrd.50700>, 2013.

687 Charlson, R. J., Schwartz, S. E., Hales, J. M., Cess, R. D., Coakley Jr, J. A., Hansen, J.
688 E., Hofmann, D. J.: Climate forcing by anthropogenic aerosols, *Science.*,
689 255(5043), 423–430, <https://doi.org/10.1126/science.255.5043.423>, 1992.

690 Chen, Y., Haywood, J., Wang, Y., Malavelle, F., Jordan, G., Partridge, D., Fieldsend, J.,
691 Leeuw, J. D., Schmidt, A., Cho, N., Oreopoulos, L., Platnick, S., Grosvenor, D.,
692 Field, P., Lohmann, U.: Machine learning reveals climate forcing from aerosols is
693 dominated by increased cloud cover, *Nature Geoscience.*, 15(8), 609–614,
694 <https://doi.org/10.1038/s41561-022-01027-9>, 2022a.

695 Chen, L., Zhang, F., Zhang, D., Wang, X., Song, W., Liu, J., Ren, J., Jiang, S., Li, X.,
696 and Li, Z.: Measurement report: Hygroscopic growth of ambient fine particles
697 measured at five sites in China, *Atmospheric Chemistry and Physics.*, 22, 6773-
698 6786, <https://doi.org/10.5194/acp-22-6773-2022>, 2022b.

699 Ching, J., Zaveri, R. A., Easter, R. C., Riemer, N., Fast, J. D.: A three-dimensional
700 sectional representation of aerosol mixing state for simulating optical properties
701 and cloud condensation nuclei, *Journal of Geophysical Research: Atmospheres.*,
702 121(10), 5912–5929, <https://doi.org/10.1002/2015JD024323>, 2016.

703 Ching, J., Fast, J., West, M., Riemer, N.: Metrics to quantify the importance of mixing
704 state for CCN activity, *Atmospheric Chemistry and Physics.*, 17(12), 7445–7458,
705 <https://doi.org/10.5194/acp-17-7445-2017>, 2017.

706 Ching, J., Adachi, K., Zaizen, Y., Igarashi, Y., Kajino, M.: Aerosol mixing state revealed
707 by transmission electron microscopy pertaining to cloud formation and human
708 airway deposition, *npj Climate and Atmospheric Science.*, 2(1), 22, <https://doi.org/10.1038/s41612-019-0081-9>, 2019.

710 Collins, D. B., Ault, A. P., Moffet, R. C., Ruppel, M. J., Cuadra-Rodriguez, L. A.,
711 Guasco, T. L., Corrigan, C. E., Pedler, B. E., Azam, F., Aluwihare, L. I., Bertram,
712 T. H., Roberts, G. C., Grassian, V. H., Prather, K. A.: Impact of marine
713 biogeochemistry on the chemical mixing state and cloud forming ability of nascent

714 sea spray aerosol, *Journal of Geophysical Research: Atmospheres.*, 118(15), 8553–
715 8565, <https://doi.org/10.1002/jgrd.50598>, 2013.

716 Cheung, H. C., Chou, C. C. K., Lee, C. S. L., Kuo, W. C., Chang, S. C.: Hygroscopic
717 properties and cloud condensation nuclei activity of atmospheric aerosols under
718 the influences of Asian continental outflow and new particle formation at a coastal
719 site in eastern Asia, *Atmospheric Chemistry and Physics.*, 20(10), 5911–5922,
720 <https://doi.org/10.5194/acp-20-5911-2020>, 2020.

721 Cai, J., Chu, B., Yao, L., Yan, C., Heikkinen, L. M., Zheng, F., Li, C., Fan, X., Zhang,
722 S., Yang, D., Wang, Y., Kokkonen, T. V., Chan, T., Zhou, Y., Dada, L., Liu, Y., He,
723 H., Paasonen, P., Kujansuu, J. T., Petäjä, T., Mohr, C., Kangasluoma, J., Bianchi,
724 F., Sun, Y., Croteau, P. L., Worsnop, D. R., Kerminen, V. M., Du, W., Kulmala, M.,
725 & Daellenbach, K. R.: Size-segregated particle number and mass concentrations
726 from different emission sources in urban Beijing, *Atmospheric Chemistry and*
727 *Physics.*, 20(21), 12721–12740, <https://doi.org/10.5194/acp-20-12721-2020>, 2020.

728 Dusek, U., Frank, G. P., Hildebrandt, L., Curtius, J., Schneider, J., Walter, S., Chand,
729 D., Drewnick, F., Hings, S., Jung, D., Borrmann, S., Andreae, M. O.: Size matters
730 more than chemistry for cloud-nucleating ability of aerosol particles, *Science.*, 312
731 (5778), 1375–1378, <https://doi.org/10.1126/science.1125261>, 2006.

732 DeCarlo, P. F., Kimmel, J. R., Trimborn, A., Northway, M. J., Jayne, J. T., Aiken, A. C.,
733 Gonin, M., Fuhrer, K., Horvath, T., Docherty, K. S., Worsnop, D. R., Jimenez, J.
734 L.: Field-deployable, high-resolution, time of-flight aerosol mass spectrometer,
735 *Analytical Chemistry.*, 78, 8281–8289, <https://doi.org/10.1021/ac061249n>, 2006.

736 Ervens, B., Cubison, M. J., Andrews, E., Feingold, G., Ogren, J. A., Jimenez, J. L.,
737 Quinn, P. K., Bates, T. S., Wang, J., Zhang, Q., Coe, H., Flynn, M., Allan, J. D.:
738 CCN predictions using simplified assumptions of organic aerosol composition and
739 mixing state: a synthesis from six different locations, *Atmospheric Chemistry and*
740 *Physics.*, 10(10), 4795–4807, <https://doi.org/10.5194/acp-10-4795-2010>, 2010.

741 Fierce, L., Onasch, T. B., Cappa, C. D., Mazzoleni, C., China, S., Bhandari, J.,
742 Davidovits, P., Fischer, D. A., Helgestad, T., Lambe, A. T., et al.: Radiative

743 absorption enhancements by black carbon controlled by particle-to-particle
744 heterogeneity in composition, *P. Natl. Acad. Sci. USA*, 117, 5196–5203,
745 <https://doi.org/10.1073/pnas.1919723117>, 2020.

746 Fan, X., Liu, J., Zhang, F., Chen, L., Collins, D., Xu, W., Jin, X., Ren, J., Wang, Y., Wu,
747 H., Li, S., Sun, Y., Li, Z.: Contrasting size-resolved hygroscopicity of fine particles
748 derived by HTDMA and HR-ToF-AMS measurements between summer and
749 winter in Beijing: the impacts of aerosol aging and local emissions, *Atmospheric
750 Chemistry and Physics*, 20(2), 915–929, <https://doi.org/10.5194/acp-20-915-2020>,
751 2020.

752 Gysel, M., Mcfiggans, G. B., Coe, H.: Inversion of tandem differential mobility
753 analyser (TDMA) measurements, *Journal of Aerosol Science*, 40(2), 134–151,
754 <https://doi.org/10.1016/j.jaerosci.2008.07.013>, 2009.

755 Hughes, M., Kodros, J. K., Pierce, J. R., West, M., Riemer, N.: Machine learning to
756 predict the global distribution of aerosol mixing state metrics, *Atmosphere*, 9(1),
757 15, <https://doi.org/10.3390/atmos9010015>, 2018.

758 Huang, R. J., Zhang, Y., Bozzetti, C., Ho, K. F., Cao, J. J., Han, Y., Daellenbach, K. R.,
759 Slowik, J. G., Platt, S. M., Canonaco, F., Zotter, P., Wolf, R., Pieber, S. M., Bruns,
760 E. A., Crippa, M., Ciarelli, G., Piazzalunga, A., Schwikowski, M., Abbaszade, G.,
761 Schnelle-Kreis, J., Zimmermann, R., An, Z., Szidat, S., Baltensperger, U., Haddad,
762 I. E., Prévôt, A. S.: High secondary aerosol contribution to particulate pollution
763 during haze events in China, *Nature*, 514(7521), 218–222, [https://doi.org/
764 10.1038/nature13774](https://doi.org/10.1038/nature13774), 2014.

765 IPCC. Summary for Policymakers. In *Climate Change 2021: The Physical Science
766 Basis. Contribution of Working Group I to the Sixth Assessment Report of the
767 Intergovernmental Panel on Climate Change*; Cambridge University Press:
768 Cambridge, United Kingdom and New York, NY, USA, 2021.

769 Liu, P., Song, M., Zhao, T., Gunthe, S. S., Ham, S., He, Y., Qin, Y., Gong, Z., Amorim,
770 C. J., Bertram, K. A., Martin, S. T.: Resolving the mechanisms of hygroscopic
771 growth and cloud condensation nuclei activity for organic particulate matter,

772 Nature communications., 9(1), 4076, <https://doi.org/10.1038/s41467-018-06622->
773 2, 2018.

774 Liu, J., Zhang, F., Ren, J., Chen, L., Zhang, A., Wang, Z., Zou, S., Xu, H., Yue, X.: The
775 evolution of aerosol mixing state derived from a field campaign in Beijing:
776 implications for particle aging timescales in urban atmospheres, *Atmospheric*
777 *Chemistry and Physics.*, 25(9), 5075–5086, <https://doi.org/10.5194/acp-25-5075->
778 2025, 2025.

779 Liu, Y., Lin, T., Zhang, J., Wang, F., Huang, Y., Wu, X., Ye, H., Zhang, G., Cao, X., and
780 de Leeuw, G.: Opposite effects of aerosols and meteorological parameters on
781 warm clouds in two contrasting regions over eastern China, *Atmospheric*
782 *Chemistry and Physics.*, 24, 4651–4673, <https://doi.org/10.5194/acp-24-4651->
783 2024, 2024.

784 Lance, S., Nenes, A., Medina, J., Smith, J. N.: Mapping the operation of the DMT
785 continuous flow CCN counter, *Aerosol Science and Technology.*, 40(4), 242–254,
786 <https://doi.org/10.1080/02786820500543290>, 2006.

787 Manavi, S. E. I., Aktypis, A., Siouti, E., Skyllakou, K., Myriokefalitakis, S., Kanakidou,
788 M., Pandis, S. N.: Atmospheric aerosol spatial variability: Impacts on air quality
789 and climate change, *One Earth.*, 8(3),
790 <https://doi.org/10.1016/j.oneear.2025.101237>, 2025.

791 Ovadnevaite, J., Ceburnis, D., Leinert, S., Dall'Osto, M., Canagaratna, M., O'Doherty,
792 S., Berresheim, H., O'Dowd, C.: Submicron NE Atlantic marine aerosol chemical
793 composition and abundance: Seasonal trends and air mass categorization, *Journal*
794 *of Geophysical Research: Atmospheres.*, 119, 11850–11863,
795 <https://doi.org/10.1002/2013JD021330>, 2014.

796 Petters, M. D., Kreidenweis, S. M.: A single parameter representation of hygroscopic
797 growth and cloud condensation nucleus activity, *Atmospheric Chemistry and*
798 *Physics.*, 7(8), 1961–1971, <https://doi.org/10.5194/acp-7-1961-2007>, 2007.

799 Padró, L. T., Moore, R. H., Zhang, X., Rastogi, N., Weber, R. J., and Nenes, A.: Mixing
800 state and compositional effects on CCN activity and droplet growth kinetics of

801 size-resolved CCN in an urban environment, *Atmospheric Chemistry and Physics*,
802 2012, 12, 10239–10255, <https://doi.org/10.5194/acp-12-10239-2012>, 2012.

803 Rosenfeld, D., Zhu, Y., Wang, M., Zheng, Y., Goren, T., Yu, S.: Aerosol- driven droplet
804 concentrations dominate coverage and water of oceanic low-level clouds, *Science*,
805 363(6427), <https://doi.org/10.1126/science.aay4194>, 2019.

806 Riemer, N., Ault, A. P., West, M., Craig, R. L., Curtis, J. H.: Aerosol mixing state:
807 Measurements, modeling, and impacts, *Reviews of Geophysics*, 57(2), 187–249,
808 <https://doi.org/10.1029/2018RG000615>, 2019.

809 Ren, J., Zhang, F., Wang, Y., Collins, D., Fan, X., Jin, X., Xu, W., Sun, Y., Cribb, M.,
810 Li, Z.: Using different assumptions of aerosol mixing state and chemical
811 composition to predict CCN concentrations based on field measurements in urban
812 Beijing, *Atmospheric Chemistry and Physics*, 18(9), 6907–6921,
813 <https://doi.org/10.5194/acp-18-6907-2018> 2018.

814 Ramachandran, S., Srivastava, R.: Mixing states of aerosols over four environmentally
815 distinct atmospheric regimes in Asia: coastal, urban, and industrial locations
816 influenced by dust, *Environmental Science and Pollution Research*, 23, 11109–
817 11128, <https://doi.org/10.1007/s11356-016-6254-8>, 2016.

818 Ren, J., Zhang, F., Chen, L., Cao, G., Liu, M., Li, X., Wu, H., Cheng, Y., and Li, Z.:
819 Identifying the hygroscopic properties of fine aerosol particles from diverse
820 sources in urban atmosphere and the applicability in prediction of cloud nuclei,
821 *Atmos. Environ.*, 298, 119615, <https://doi.org/10.1016/j.atmosenv.2023.119615>,
822 2023.

823 Riemer, N. and West, M.: Quantifying aerosol mixing state with entropy and diversity
824 measures, *Atmospheric Chemistry and Physics*, 13, 11423–11439,
825 <https://doi.org/10.5194/acp-13-11423-2013>, 2013.

826 Rose, D., Gunthe, S. S., Mikhailov, E., Frank, G. P., Dusek, U., Andreae, M. O., Pöschl,
827 U.: Calibration and measurement uncertainties of a continuous-flow cloud
828 condensation nuclei counter (DMT-CCNC): CCN activation of ammonium sulfate
829 and sodium chloride aerosol particles in theory and experiment, *Atmospheric*

830 Chemistry and Physics., 8(5), 1153–1179, <https://doi.org/10.5194/acp-8-1153->
831 2008, 2008.

832 Shrivastava, M., Cappa, C. D., Fan, J., Goldstein, A. H., Guenther, A. B., Jimenez, J.
833 L., Kuang, C., Laskin, A., Martin, S. T., Ng, N. L., Petaja, T., Pierce, J. R., Rasch,
834 P. J., Roldin, P., Seinfeld, J. H., Shilling, J., Smith, J. N., Thornton, J. A., Volkamer,
835 R., Wang, J., Worsnop, D. R., Zaveri, R. A., Zelenyuk, A., Zhang, Q.: Recent
836 advances in understanding secondary organic aerosol: Implications for global
837 climate forcing, *Reviews of Geophysics.*, 55(2), 509–559,
838 <https://doi.org/10.1002/2016RG000540>, 2017.

839 Stevens, R., and Dastoor, A.: A Review of the Representation of Aerosol Mixing State
840 in Atmospheric Models, *Atmosphere.*, 10, 168,
841 <https://doi.org/10.3390/atmos10040168>, 2019.

842 Spitieri, C., Gini, M., Gysel-Beer, M., and Eleftheriadis, K.: Annual cycle of
843 hygroscopic properties and mixing state of the suburban aerosol in Athens, Greece,
844 *Atmospheric Chemistry and Physics.*, 23, 235–249, <https://doi.org/10.5194/acp->
845 23-235-2023, 2023.

846 Sotiropoulou, R. E. P., Nenes, A., Adams, P. J., Seinfeld, J. H.: Cloud condensation
847 nuclei prediction error from application of Köhler theory: Importance for the
848 aerosol indirect effect, *Journal of Geophysical Research: Atmospheres.*, 112(D12),
849 <https://doi.org/10.1029/2006JD007834>, 2007.

850 Schill, S. R., Collins, D. B., Lee, C., Morris, H. S., Novak, G. A., Prather, K. A., Quinn,
851 P. K., Sultana, C. M., Tivanski, A. V., Zimmermann, K., Cappa, C. D., Bertram, T.
852 H.: The impact of aerosol particle mixing state on the hygroscopicity of sea spray
853 aerosol, *ACS central science.*, 1(3), 132-141,
854 <https://doi.org/10.1021/acscentsci.5b00174>, 2015.

855 Shi, Z., Vu, T., Kotthaus, S., Harrison, R. M., Grimmond, S., Yue, S., Zhu, T., Lee, J.,
856 Han, Y., Demuzere, M., Dunmore, R. E., Ren, L., Liu, D., Wang, Y., Wild, O.,
857 Allan, J., Acton, W. J., Barlow, J., Barratt, B., Beddows, D., Bloss, W. J., Calzolari,
858 G., Carruthers, D., Carslaw, D. C., Chan, Q., Chatzidiakou, L., Chen, Y., Crilley,

859 L., Coe, H., Dai, T., Doherty, R., Duan, F., Fu, P., Ge, B., Ge, M., Guan, D.,
860 Hamilton, J. F., He, K., Heal, M., Heard, D., Hewitt, C. N., Hollaway, M., Hu, M.,
861 Ji, D., Jiang, X., Jones, R., Kalberer, M., Kelly, F. J., Kramer, L., Langford, B.,
862 Lin, C., Lewis, A. C., Li, J., Li, W., Liu, H., Liu, J., Loh, M., Lu, K., Lucarelli, F.,
863 Mann, G., McFiggans, G., Miller, M. R., Mills, G., Monk, P., Nemitz, E., O'Connor,
864 F., Ouyang, B., Palmer, P. I., Percival, C., Popoola, O., Reeves, C., Rickard, A. R.,
865 Shao, L., Shi, G., Spracklen, D., Stevenson, D., Sun, Y., Sun, Z., Tao, S., Tong, S.,
866 Wang, Q., Wang, W., Wang, X., Wang, X., Wang, Z., Wei, L., Whalley, L., Wu, X.,
867 Wu, Z., Xie, P., Yang, F., Zhang, Q., Zhang, Y., Zhang, Y., and Zheng, M.:
868 Introduction to the special issue “In-depth study of air pollution sources and
869 processes within Beijing and its surrounding region (APHH-Beijing)”,
870 *Atmospheric Chemistry and Physics*, 19, 7519–7546, [https://doi.org/10.5194/acp-](https://doi.org/10.5194/acp-19-7519-2019)
871 [19-7519-2019](https://doi.org/10.5194/acp-19-7519-2019), 2019.

872 Stokes, R. H., Robinson, R. A.: Interactions in aqueous nonelectrolyte solutions. I.
873 Solute-Solvent equilibria, *Journal of Physical Chemistry*, 70(7), 2126–2130,
874 <https://doi.org/10.1021/j100879a010>, 1966.

875 Tao, J., Kuang, Y., Ma, N., Hong, J., Sun, Y., Xu, W., Zhang, Y., He, Y., Luo, Q., Xie,
876 L., Su, H., and Cheng, Y.: Secondary aerosol formation alters CCN activity in the
877 North China Plain, *Atmospheric Chemistry and Physics*, 21, 7409–7427,
878 <https://doi.org/10.5194/acp-21-7409-2021>, 2021.

879 Tao, J., Luo, B., Xu, W., Zhao, G., Xu, H., Xue, B., Zhai, M., Xu, W., Zhao, H., Ren,
880 S., Zhou, G., Liu, L., Kuang, Y., and Sun, Y.: Markedly different impacts of
881 primary emissions and secondary aerosol formation on aerosol mixing states
882 revealed by simultaneous measurements of CCNC, H(V)TDMA, and SP2,
883 *Atmospheric Chemistry and Physics*, 24, 9131–9154, [https://doi.org/10.5194/acp-](https://doi.org/10.5194/acp-24-9131-2024)
884 [24-9131-2024](https://doi.org/10.5194/acp-24-9131-2024), 2024.

885 Virtanen, A., Joutsensaari, J., Kokkola, H., Partridge, G. D., Blichner, S., Seland, Ø.,
886 Holopainen, E., Tovazzi, E., Lipponen, A., Mikkonen, S., Leskinen, A., Hyvärinen,
887 A., Zieger, P., Krejci, R., Ekman, A. M. L., Riipinen, I., Quaas, J., Romakkaniemi,

888 S.: High sensitivity of cloud formation to aerosol changes, *Nature Geoscience.*, 1–
889 7, <https://doi.org/10.1038/s41561-025-01662-y>, 2025.

890 Winkler, P.: The growth of atmospheric aerosol particles as a function of the relative
891 humidity—II. An improved concept of mixed nuclei, *Journal of Aerosol Science.*,
892 4(5), 373–387, [https://doi.org/10.1016/0021-8502\(73\)90027-X](https://doi.org/10.1016/0021-8502(73)90027-X), 1973.

893 Wang, J., Cubison, M. J., Aiken, A. C., Jimenez, J. L., Collins, D. R.: The importance
894 of aerosol mixing state and size-resolved composition on CCN concentration and
895 the variation of the importance with atmospheric aging of aerosols, *Atmospheric
896 Chemistry and Physics.*, 10(15), 7267–7283, [https://doi.org/10.5194/acp-10-7267-](https://doi.org/10.5194/acp-10-7267-2010)
897 2010, 2010.

898 Wang, Y., Li, Z., Zhang, R., Jin, X., Xu, W., Fan, X., et al.: Distinct ultrafine- and
899 accumulation-mode particle properties in clean and polluted urban environments,
900 *Geophysical Research Letters.*, 46, 10,918–10,925,
901 <https://doi.org/10.1029/2019GL084047>, 2019.

902 Xu, W., Ovadnevaite, J., Fossum, K. N., Lin, C., Huang, R. J., Ceburnis, D., O’Dowd,
903 C.: Sea spray as an obscured source for marine cloud nuclei, *Nature Geoscience.*,
904 15(4), 282–286, <https://doi.org/10.1038/s41561-022-00917-2>, 2022.

905 Xu, W., Ovadnevaite, J., Fossum, K. N., Huang, R. J., Huang, D., Zhong, H., Gu, Y.,
906 Lin, C., Huang, C., O’Dowd, C., Ceburnis, D.: Condensation of organic-inorganic
907 vapours governs the production of ultrafine secondary marine cloud nuclei,
908 *Communications Earth & Environment.*, 5(1), 359,
909 <https://doi.org/10.1038/s43247-024-01519-z>, 2024.

910 Xu, W., Ovadnevaite, J., Fossum, K. N., Lin, C., Huang, R. J., O’Dowd, C., Ceburnis,
911 D.: Aerosol hygroscopicity and its link to chemical composition in the coastal
912 atmosphere of Mace Head: marine and continental air masses, *Atmospheric
913 Chemistry and Physics.*, 20(6), 3777–3791, [https://doi.org/10.5194/acp-20-3777-](https://doi.org/10.5194/acp-20-3777-2020)
914 2020, 2020.

915 Xu, W., Ovadnevaite, J., Fossum, K. N., Lin, C., Huang, R.-J., O’Dowd, C., Ceburnis,
916 D.: Seasonal trends of aerosol hygroscopicity and mixing state in clean marine and

917 polluted continental air masses over the Northeast Atlantic, *Journal of Geophysical*
918 *Research: Atmospheres.*, 126, e2020JD033851,
919 <https://doi.org/10.1029/2020JD033851>, 2021a.

920 Xu, W., Sun, Y., Wang, Q., Zhao, J., Wang, J., Ge, X., Xie, C., Zhou, W., Du, W., Li, J.,
921 Fu, P., Wang, Z., Worsnop, D. R., Coe, H.: Changes in aerosol chemistry from
922 2014 to 2016 in winter in Beijing: Insights from high-resolution aerosol mass
923 spectrometry, *Journal of Geophysical Research: Atmospheres.*, 124, 1132–1147,
924 <https://doi.org/10.1029/2018JD029245>, 2019.

925 Xie, C., He, Y., Lei, L., Zhou, W., Liu, J., Wang, Q., Xu, W., Qiu, Y., Zhao, J., Sun, J.,
926 Li, L., Li, M., Zhou, Z., Fu, P., Wang, Z., Sun, Y.: Contrasting mixing state of black
927 carbon-containing particles in summer and winter in Beijing, *Environmental*
928 *Pollution.*, 263, 114455, <https://doi.org/10.1016/j.envpol.2020.114455>, 2020.

929 Xu, W., Fossum, K. N., Ovadnevaite, J., Lin, C., Huang, R. J., O'Dowd, C., Ceburnis,
930 D.: The impact of aerosol size-dependent hygroscopicity and mixing state on the
931 cloud condensation nuclei potential over the north-east Atlantic, *Atmospheric*
932 *Chemistry and Physics.*, 21(11), 8655–8675, [https://doi.org/10.5194/acp-21-8655-](https://doi.org/10.5194/acp-21-8655-2021)
933 [2021](https://doi.org/10.5194/acp-21-8655-2021), 2021b.

934 Ye, Q., Gu, P., Li, H. Z., Robinson, E. S., Lipsky, E. M., Kaltsonoudis, C., Lee, A. K.
935 Y., Apte, J. S., Robinson, A. L., Sullivan, R. C., Presto, A. A., Donahue, N. M.:
936 Spatial variability of sources and mixing state of atmospheric particles in a
937 metropolitan area, *Environmental Science & Technology.*, 52, 6807–6815,
938 <https://doi.org/10.1021/acs.est.8b01011>, 2018.

939 Yuan, L., and Zhao, C.: Quantifying particle-to-particle heterogeneity in aerosol
940 hygroscopicity, *Atmospheric Chemistry and Physics.*, 23, 3195–3205,
941 <https://doi.org/10.5194/acp-23-3195-2023>, 2023.

942 Yang, F., Chen, H., Du, J., Yang, X., Gao, S., Chen, J., Geng, F.: Evolution of the mixing
943 state of fine aerosols during haze events in Shanghai, *Atmospheric Research.*, 104:
944 193-201, <https://doi.org/10.1016/j.atmosres.2011.10.005>, 2012.

945 Zheng, Z., Curtis, J. H., Yao, Y., Gasparik, J. T., Anantharaj, V. G., Zhao, L., West, M.,

946 Riemer, N.: Estimating submicron aerosol mixing state at the global scale with
947 machine learning and Earth system modeling, *Earth and Space Science.*, 8(2),
948 e2020EA001500, <https://doi.org/10.1029/2020EA001500>, 2021a.

949 Zheng, Z., West, M., Zhao, L., Ma, P.-L., Liu, X., and Riemer, N.: Quantifying the
950 structural uncertainty of the aerosol mixing state representation in a modal model,
951 *Atmospheric Chemistry and Physics.*, 21, 17727–17741,
952 <https://doi.org/10.5194/acp-21-17727-2021>, 2021b.

953 Zhao, G., Tan, T., Zhu, Y., Hu, M., and Zhao, C.: Method to quantify black carbon
954 aerosol light absorption enhancement with a mixing state index, *Atmospheric
955 Chemistry and Physics.*, 21, 18055–18063, [https://doi.org/10.5194/acp-21-18055-
956 2021](https://doi.org/10.5194/acp-21-18055-2021), 2021.

957 Zdanovskii, A.: New methods for calculating solubilities of electrolytes in
958 multicomponent systems, *Zh. Fiz. Khim. C*, 22, 1475–1485, 1948.

959 Zhong, H., Huang, R. J., Lin, C., Xu, W., Duan, J., Gu, Y., Huang, W., Ni, H.; Zhu, C.,
960 You, Y., Wu, Y., Zhang, R., Ovadnevaite, J., Ceburnis, D., O'Dowd, C.:
961 Measurement report: On the contribution of long-distance transport to the
962 secondary aerosol formation and aging, *Atmospheric Chemistry and Physics.*, 22,
963 9513–9524, <https://doi.org/10.5194/acp-22-9513-2022>, 2022.